

PAPER • OPEN ACCESS

Errors in single pixel laser imaging emerging from spatial size limits in the bucket detector

To cite this article: Dennis Scheidt and Pedro A Quinto-Su 2025 J. Opt. 27 015605

View the article online for updates and enhancements.

You may also like

- Radiation damage free ghost diffraction with atomic resolution
 Zheng Li, Nikita Medvedev, Henry N Chapman et al.
- A review of single and multiple optical image encryption techniques
 Abdurrahman Hazer and Remzi Yldrm
- High-performance deep-learning based polarization computational ghost imaging with random patterns and orthonormalization
 Chenxiang Xu, Dekui Li, Xueqiang Fan et

J. Opt. 27 (2025) 015605 (10pp)

Errors in single pixel laser imaging emerging from spatial size limits in the bucket detector

Dennis Scheidt^{1,2,*} and Pedro A Quinto-Su¹

- ¹ Instituto de Ciencias Nucleares, Universidad Nacional Autónoma de México, Cto. Exterior S/N, C.U., Coyoacán, Mexico City, 04510 Mexico City, Mexico
- ² Institute for Neuroscience and Medicine 1, Forschungszentrum Jülich, Wilhelm-Johnen-Straße, Jülich 52428, NRW, Germany

E-mail: d.scheidt@fz-juelich.de and pedro.quinto@nucleares.unam.mx

Received 23 July 2024, revised 13 October 2024 Accepted for publication 28 November 2024 Published 13 December 2024



Abstract

In single pixel imaging (SPI) an image is sampled with an orthogonal basis projected by a programmable optical element like a digital micromirror array or a spatial light modulator. The reflected or diffracted light is collected by a lens and measured with a photodiode or bucket detector. In this work we demonstrate that SPI of laser light fields can exhibit cross talk with its phase when the bucket detector is not sufficiently large (i.e. fast photodiodes) and does not integrate the full spectrum of each basis element. In that regime, structured phases can emerge from errors in the optical or light collection system (i.e. misaligned optical elements or aberrations) and can appear in the reconstructed amplitude image. We show this behavior in simulations and experiments where the reconstructed amplitude image will exhibit phase cross-talk if the detector size is smaller than between 50% and 75% of the maximum area spanned by the projected spectrum of the measurement basis. This is important because photodiodes with a fast response time have a small effective area.

Supplementary material for this article is available online

Keywords: single pixel imaging, digital holography, crosstalk, spatial light modulator, imaging artifacts

1

1. Introduction

Single pixel imaging (SPI) was introduced in 2006 by Duarte *et al* [1], where they demonstrated the ability to capture an image with a single photodetector, in contrast to regular digital cameras that use CCD or CMOS detectors containing millions of individual sensors or pixels. Their approach projected an

Original Content from this work may be used under the terms of the Creative Commons Attribution 4.0 licence. Any further distribution of this work must maintain attribution to the author(s) and the title of the work, journal citation and DOI.

image into a digital micromirror array (DMD) that activates groups of micromirrors representing elements of an orthogonal basis. The reflected light was collected by a lens and detected by a single photodiode (bucket detector) placed at the lens' focal spot. In this way, by sampling all the basis elements and recording the intensity of each basis element, it is possible to reconstruct the image. This approach has the advantage that it enables to obtain images at wavelengths that are outside regular CCD or CMOS sensors. Furthermore, it was also shown that compressive sensing could be used to reconstruct an image by only sampling a subset of the vectors contained in the measurement basis [1–3].

The theoretical foundation for SPI has already been established in the 1990s by Klyshko and Shih [4, 5], called Ghost Imaging, where the spatial correlation between two detected

^{*} Author to whom any correspondence should be addressed.

J. Opt. 27 (2025) 015605

photons encodes the spatial information of the image. Based on this, the group of Tajahuerce used computational ghost imaging (CGI) to measure the amplitude and phase of objects with holographic techniques [6]. CGI does not require correlated photon pairs due to the use of a SLM that encodes a spatial pattern onto the light field [7]. While the key difference between SPI and CGI lies in the illumination of the object, for the purposes of this article, we will treat them as equivalent [7, 8]. Later, similar approaches were used to measure the phase of laser fields using the same SPI approach of sampling the field with an orthogonal basis combined with interferometry [9, 10]. In contrast to the bucket detector approach of SPI, the intensities are measured at a single point (single pixel in a camera) or selecting the light from a small area with a spatial filter followed by a photodiode [11, 12].

In a previous work, we examined the influence of the phase onto the reconstructed amplitude for complex SPI, i.e. measuring the amplitude and phase with interferometry [13].

In this work we investigate the effect of the bucket detector size on the resulting reconstructed image (amplitude-only), relative to the area spanned by the Fourier spectrum of the elements of the sampling basis. This is important because fast photodiodes can have very small effective areas. The effect of the photodiode size has been investigated in the context of signal to noise ratio [14, 15]. Here we look at another fundamental aspect of SPI as a function of the detector area. We use a complete Hadamard basis to sample and reconstruct an image and show that errors like aberrations caused by phase components contained in the field can appear in the reconstructed image due to cross-talk emerging from incomplete integration by the bucket detector of the light projected by the elements of the sampling basis. In particular, we study three cases of SPI to reconstruct the amplitude: Image encoded in the amplitude (constant phase), complex image (image in amplitude and image in phase) and image encoded in amplitude with errors in the light collection system (tilted lens, aberrations).

2. SPI

Let's consider a complex field u that is represented by a vector with N components. An image of the complex field will only include the intensity and the resulting image is represented by a vector $x \propto |u|^2$. The image $|u|^2$ is sampled by an orthogonal basis Φ ($N \times N$ matrix), where the orthogonal ($1 \times N$) vectors Φ_l ($l \in [1,N]$) are the rows of that matrix. The projections of the image in each orthogonal basis element are $y = \Phi u$, where y is the vector of the integrated measured intensity for each vector that makes the orthogonal basis.

Most SPI implementations use the Hadamard basis $\Phi = H$ because it spans the full effective area of the programmable optical element (i.e. it contains no zeros), in contrast to the canonical basis represented by the identity matrix I ($\Phi = I$). The Hadamard matrix has the following property $HH^T = H^2 = NI$. Many experiments divide the Hadamard matrix into a positive part and a negative part $H = H^+ - H^-$, so that $H^+ = (H+1)/2$ and $H^- = -(H-1)/2$ (both binary matrices containing zeros and ones). By combining the two corresponding

measurement vectors y^+ and y^- , respectively, the acquired signal reads: $y = y^+ - y^-$. The image is then reconstructed with x = Hy = HHu = Nu.

3. Field and basis encoding

Lets define the discrete complex light field at the surface of a SLM (or DMD) with spatial coordinates (X,Y): $u(X,Y) = A(X,Y) \exp(i\phi(X,Y))$. The field is resized into a $\sqrt{N} \times \sqrt{N}$ square grid made of N superpixels. The same resizing procedure is done for the 1-d positive and negative vector elements of the bases Φ_l^\pm where $l \in [1,N]$ denotes the lth measurement vector of the basis. In this way, the projection of the field on the basis element Φ_l^\pm is encoded with $\Phi_l^\pm(X,Y)\odot u(X,Y)$, where \odot is the element-wise multiplication. Since that new field is also encoded in the same area of the SLM, it is also a function of the same spatial coordinates.

The light diffracted (or reflected) by the new encoded field can be collected by a lens (focal length f) focusing it on a photodiode (bucket detector) that integrates the intensity of each basis element. The focal plane coordinates are given by the spatial frequencies (k_X, k_Y) due to the Fourier transform relation between the surface of the SLM and the focal plane. The focused pattern for a positive/negative basis element is the 2-dimensional Fourier transform of the field projected at the surface of the SLM is:

$$\mathcal{F}\left\{\Phi_{l}^{\pm}\left(X,Y\right)\odot u\left(X,Y\right)\right\}_{k_{X},k_{Y}}$$

$$=\iint_{\Delta X,\Delta Y} dXdY \,\Phi_{l}^{\pm}\left(X,Y\right)u\left(X,Y\right)$$

$$\exp\left(-2\pi i\left(k_{X}X+k_{Y}Y\right)\right) \,. \tag{1}$$

 \mathcal{F} denotes the 2 dimensional Fourier transform that is applied by the focusing lens with their respective frequency components $k_x = X/\lambda f$ and $k_y = Y/\lambda f$. ΔX and ΔY represent the size of the square aperture at the SLM in X and Y, respectively.

The projected intensity pattern $I(k_X, k_Y)$ at the focus is proportional to: $|\mathcal{F}\{\Phi_l^{\pm}(X, Y) \odot u(X, Y)\}_{k_X, k_Y}|^2$.

The photodiode integrates the signal over the Fourier spectrum k_X, k_Y , yielding the measured intensity as y_l^{\pm} :

$$y_{l}^{\pm} = \iint \mathrm{d}k_{x} \mathrm{d}k_{y} |\mathcal{F}\left\{\Phi_{l}^{\pm}\left(X,Y\right) \odot u\left(X,Y\right)\right\}_{k_{X},k_{Y}}|^{2}. \tag{2}$$

Writing the Fourier transforms explicitly:

$$y_{l}^{\pm} = \iint dk_{X} dk_{Y} \left[\iint_{\Delta X, \Delta Y} dX dY \Phi_{l}^{\pm}(X, Y) u(X, Y) \cdot \exp\left(-2\pi i \left(k_{X}X + k_{Y}Y\right)\right) \cdot \iint_{\Delta X, \Delta Y} dX' dY' \Phi_{l}^{\pm *}(X', Y') u^{*}(X', Y') \cdot \exp\left(2\pi i \left(k_{X}X' + k_{Y}Y'\right)\right) \right].$$
(3

Notice, that the expression between the brackets is proportional to the intensity $I(k_X, k_Y)$ depending only on the spatial

J. Opt. 27 (2025) 015605

frequencies. The spatial integrals of the Fourier transform that represent the field at the focus and its complex conjugate are done independently, so we use two sets of spatial coordinates (X, Y) and (X', Y') for the focused field and its complex conjugate, respectively. Reordering and using $u(X, Y) = A(X, Y) \exp(i\phi(X, Y))$ yields:

$$y_{l}^{\pm} = \iint_{\Delta X} dX dX' \iint_{\Delta Y} dY dY' \Phi_{l}^{\pm}(X, Y) \Phi_{l}^{\pm}(X', Y')$$

$$\cdot A(X, Y) A(X', Y') \exp(i(\phi(X, Y) - \phi(X', Y')))$$

$$\cdot \iint dk_{X} dk_{Y} \exp(-2\pi i(k_{X}(X - X') + k_{Y}(Y - Y'))) .$$
(4)

Ideally, the photodiode will collect the full spectrum, so that there is no power loss.

Evaluating the frequency integrals (dk) over the full spectrum yields:

$$\iint_{\infty} dk_X dk_Y e^{-2\pi i \left(k_X \left(X - X'\right) + k_Y \left(Y - Y'\right)\right)} = \delta \left(X - X', Y - Y'\right) ,$$
(5)

where δ is the Dirac delta function. In this way, y_l^{\pm} reduces to:

$$y_l^{\pm} = \iint_{\Delta X, \Delta Y} dX dY |\Phi_l^{\pm}(X, Y) A(X, Y)|^2, \qquad (6)$$

which is what is expected for single pixel images: The measurements for each element of the basis integrate the intensities and there is no phase information.

Note, that $\iint_{\Delta X, \Delta Y} dXdY |\Phi_l^{\pm}(X, Y)A(X, Y)|^2 = \iint_{\Delta X, \Delta Y} dXdY |\Phi_l^{\pm}(X, Y)|A(X, Y)|^2 = \iint_{\Delta X, \Delta Y} dXdY |\Phi_l^{\pm}(X, Y)|A(X, Y)|^2 = \Phi_l^{\pm}(X, Y) \cdot |A(X, Y)|^2$, because the basis $\Phi^{\pm} = H^{\pm}$ has only entries of 0 or 1. Therefore, the recovered image of image $|A|^2$ is scaled by a constant using $x = Hy = H(y^+ - y^-) = HH|A|^2 = N|A|^2$.

In the case that the bucket detector does not integrate the full spectrum, the integrals over $\mathrm{d}k$ in equation (2) are evaluated over arbitrary boundaries A and B. The k_X integral is $\int_A^B \mathrm{d}k_X \exp\left(-2\pi i k_X(X-X')\right) = -i \frac{\exp\left(-2\pi i B(X-X')\right) - \exp\left(-2\pi i A(X-X')\right)}{2\pi(X-X')}$. For the special case of a symmetric integration of the spectrum, that is $A = -B = r_k$, the expression simplifies to:

$$\int_{-r_k}^{r_k} dk_X e^{-2\pi i \left(k_X \left(X - X'\right)\right)} = 2r_k \operatorname{sinc}\left(2\pi r_k \left(X - X'\right)\right) . \quad (7)$$

Note, that with increasing r_k , the expression approaches the Dirac delta function.

Evaluating equation (4) in the case of a truncated integration over $(-r_k, r_k)$ for both k_X, k_Y (square detector with area $4r_x^2$) yields:

$$y_{l}^{\pm} = \iint_{\Delta X} dX dX' \iint_{\Delta Y} dY dY' \Phi_{l}^{\pm^{2}} A^{2}(X, Y) \cdot 4r_{k}^{2} \exp\left(i\left(\phi(X, Y) - \phi(X', Y')\right)\right) \cdot \operatorname{sinc}\left(2\pi r_{k}(X - X')\right) \operatorname{sinc}\left(2\pi r_{k}(Y - Y')\right) . \tag{8}$$

This expression is independent of the sampling basis (e.g. Gaussian, Hadamard). As a consequence of equation (8), phase crosstalk $\exp(i(\phi(X,Y)-\phi(X',Y')))$ emerges resulting in phase induced artifacts in the reconstructed image. The exception would be a basis that only contains diagonal elements (e.g. canonical) as there is no crosstalk between basis elements.

Next, we quantify the spatial size of the detector $(2r_k)$ that is needed to avoid phase cross-talk in the reconstructed image. This is done as a function of the focal length of the lens, the size of encoded field and the maximum spatial frequency reached by the measuring basis.

4. Projected pattern sizes

The maximum spatial range covered by the focused basis elements can be calculated for each direction using the 1d Fourier transform of the Hadamard elements, as the Fourier transform is separable for each dimension. The pattern with the highest spatial frequency is that of a checkerboard with the squares of length a, so the maximum spatial frequency is $f_{X\max} = 1/(2a)$.

So in one direction (X or Y) this is represented by a pulse train containing a periodic square wave with a width of a which is the length of an individual superpixel. The length of the pulse train is $L = \sqrt{N}a$. The pulse train is described by [16] as $f(X) = (\text{rect}(X/a) \otimes \text{comb}(X - 2a)) \cdot \text{rect}(X/L)$, where rect(X) and comb(X) are the rectangular and Dirac comb function, respectively. The resulting intensity is proportional to the square of the Fourier transform calculated in [16]:

$$I(f_X) \propto \sum_{m=-\infty}^{m=\infty} \left(\operatorname{sinc}(m/2) \operatorname{sinc}(La(f_X - f_{X_{\text{max}}}))^2 \right), \quad (9)$$

where $f_X = X/\lambda f$ and $m \in \mathbb{N}$. The intensity is determined by the first sinc function $\mathrm{sinc}(m/2)$ and decays rapidly with increasing m. We therefore define the extent of the spectrum with the position of the first observed peak, that occurs when the argument of the second sinc function is zero, at $f_X = f_{X\max}$ so that $1/(2a) = X/(\lambda f)$. Thus, the spatial dimension of r_k is:

$$r_k = \lambda f / (2a) . ag{10}$$

Hence, in order to eliminate phase crosstalk, we need a detector with a spatial extension of at least $2r_k$.

5. Experimental setup

The experimental setup is similar to the one described in [17] and to the original of Duarte *et al* [1] that used a DMD. In our case, the field is sampled using a SLM (Hamamatsu LCOS-SLM X10468) with a pixel size of $20 \,\mu\text{m}$. The light source is an expanded HeNe laser (wavelength $\lambda = 633 \,\text{nm}$).

The amplitude of the fields at the SLM has the shape of the expanded Gaussian beam profile or it is a 32×32 pixel image from the CIFAR-10 database [18] as depicted in figure 1(a1). An arbitrary phase defined in the same grid can be added to

create a complex field figure 1(a2). We encode two cases, only an image in the amplitude (constant phase) and complex encoding with an image in the amplitude and another image in the phase. We use the encoding method of [19] and the steps are shown in figures 1(a1)–(a4)) with a phase-only hologram figure 1(a4). In this way, we are able to probe for the phase influence on the encoded amplitude using a single SLM. Furthermore, pixel cross-talk in the hologram is reduced by applying a Gaussian filter to decrease the effect of phase discontinuities [20].

The field is encoded at the SLM in an area of 384×384 pixels yielding a square aperture with a size of $7.68 \times 7.68 \,\mathrm{mm^2}$. So the 32×32 field is resized to the square aperture resulting in superpixels that have a size of $240 \times 240 \,\mu\mathrm{m^2}$ ($12 \times 12 \,\mathrm{px^2}$). A Hadamard basis with 1024 elements is used to sample the field by sampling the positive and negative parts separately according to the $H = H^+ + H^-$. Each (1024×1) element is also reshaped to a (32×32) array and resized in the same way as the field (see figure 1(a5)). Finally, the measurement vector is directly superposed onto the hologram that creates the complex field by $\Phi_m^\pm \odot u$ (figure 1(a6)) like in [21].

The simplified experimental setup is depicted in figure 1(b). The field encoded at the SLM is focused by the first lens L_1 $(f_1 = 50 \,\mathrm{cm})$, then the beam is recollimated by L_2 $(f_2 = 15 \,\mathrm{cm})$ projecting the screen of the SLM at a distance of f_2 from L_2 spatially minimized by a factor of f_2/f_1 , so the square aperture size is now $2.304 \times 2.304 \, \text{mm}$ (effective SLM pixel size reduced to $6 \mu m$). This is followed by a third lens L_3 with $f_3 = 20 \,\mathrm{cm}$ that focuses the diffracted light (first order, spatially filtered at the first lens) into the bucket detector which in this case is a CCD camera. We use a CCD camera because it enables us to integrate the signal across different regions of interest to simulate bucket detectors with different sizes in the range of $[3.6 \times 3.6, 1440 \times 1440 \,\mu\text{m}^2]$. The width of the Hadamard pattern with the maximum spatial frequency (checkerboard pattern) is $a = 72 \,\mu\text{m}$, so that $r_k = 879 \,\mu\text{m}$. Notice that the sensitivity of a photodetector, dynamic range and response time will be different than that of an integrated signal of an area of a CCD. However, as long as the pixels are not saturated, the acquired signal will not be significantly affected [14, 15].

Figure 2(a) shows the different focused positive Hadamard basis elements H_m^+ for checkerboard-like patterns with increasing spatial frequencies. The last frame shows the projected intensity for the pattern with the highest spatial frequency H_{34}^+ that has the maximum spatial spread. We observe that the intensity pattern is made by five spots, one at the center and four near the corners. The distance from the center (horizont-al/vertical) to one of the spots at the corners is $\approx 860 \mu m$, which is consistent with the calculated r_k of $879 \mu m$.

Figure 2(b) shows the shape of the focused spots for different fields: One with a vertical phase discontinuity of π , another with a phase corresponding to a tilt and astigmatism aberration with $\phi(\rho) = \text{mod}(4\pi Z_1^1(\rho) + \pi Z_2^2(\rho), 2\pi)$ with normalized Zernike polynomials. The middle case has an arbitrary phase with the shape of a boat. Finally, figure 2(c) depicts the focused spots of beams without an added phase where the

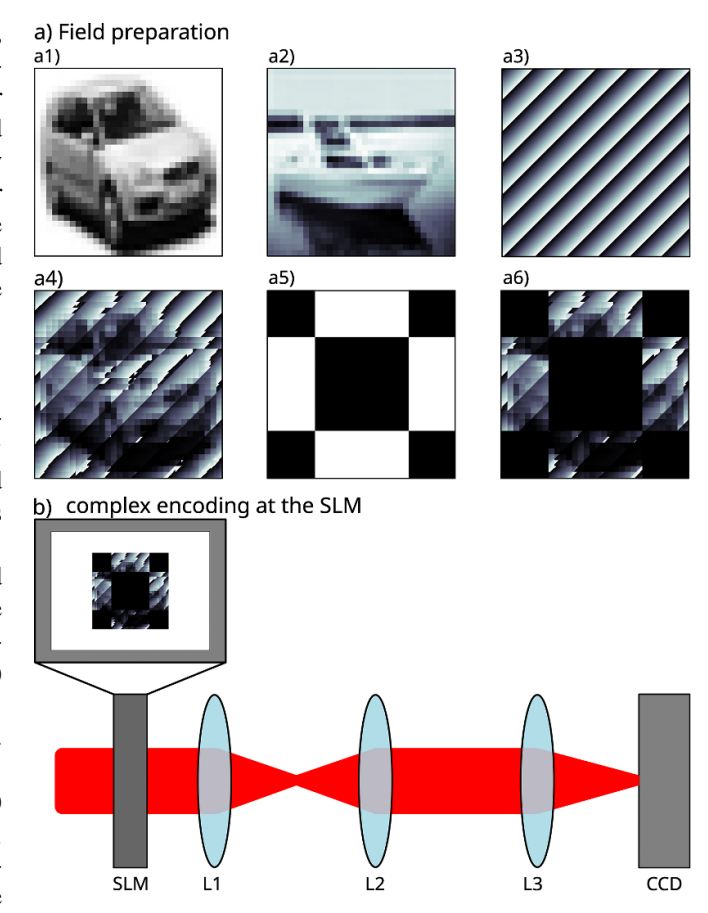


Figure 1. Field preparation and setup schematics. Inset (a) displays the preparation scheme of the complex field and measurement basis. (a1): Amplitude (image) of the field, (a2): Encoded phase, (a3): Diffraction grating (prism phase), (a4): Encoded complex field with reduced crosstalk, (a5): Binary basis element (1: white, 0: white), (a6): Complex field encoding \times basis element (b) Simplified experimental setup. The SLM is reflective but we draw it as a transmission element to simplify the setup. Lens L_1 (focal length f_1) focuses the field that is prepared with the SLM, which is then collimated by lens L_2 and refocused by lens L_3 . The distance between L_2 and L_3 is $f_2 + f_3$.

focusing lens is twisted at different angles, generating an aberration that is a mixture of tilt and astigmatism, similar to the Zernike aberration shown in 2(b). It is important to mention that as the center of the focused beam shifts slightly depending on the applied phase or twist of the lens, before starting the measurement the evaluated region of interest (ROI) in the camera is centered around the maximum of the disturbed focal spot.

6. Simulation

The experiment is simulated using the experimental parameters and the discrete versions of equations (1)–(8), where the Fourier transform is replaced by a discrete Fourier transform. The main difference is that the integrals become sums and in the case of the integrals over the full frequency spectrum (equation (5)) yield the Kronecker delta δ_{nm} instead of the Dirac delta function, yielding $y_l^{\pm} = \sum_{n,m} |\Phi_{nm} A_{nm}|^2$, where l

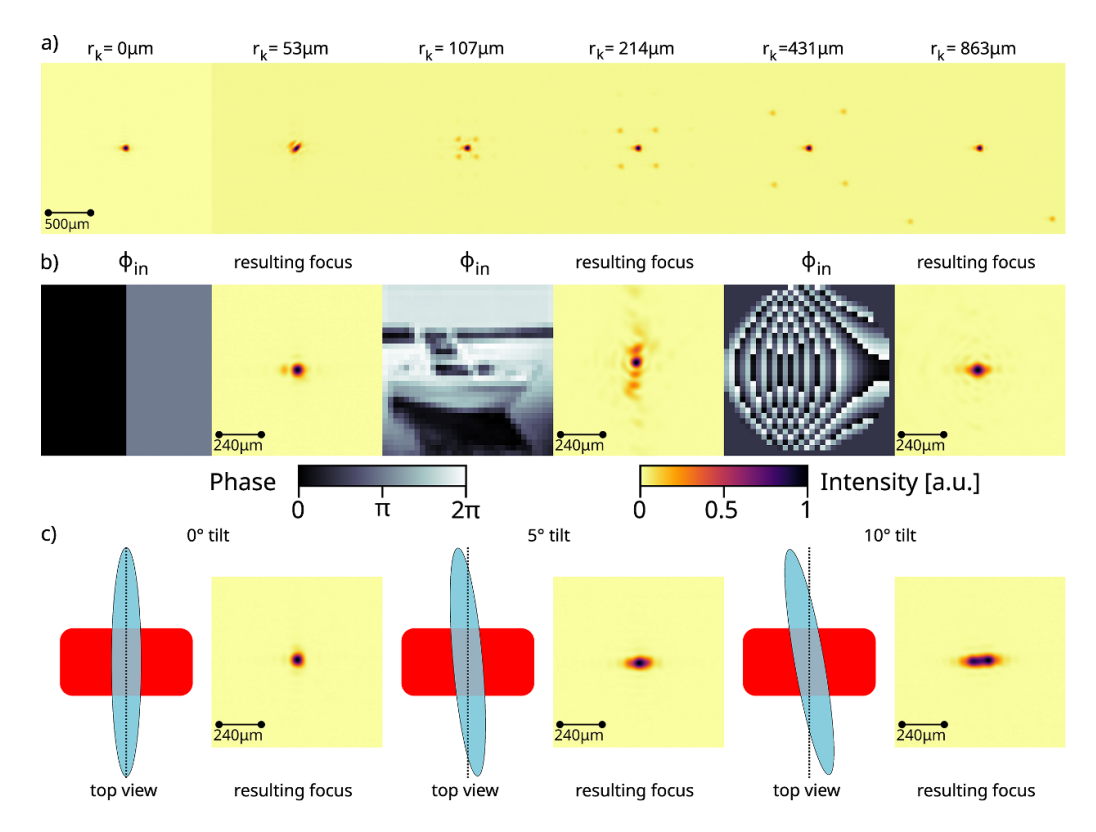


Figure 2. Spectral properties: (a) extend of the Hadamard spectrum of different basis vectors according to equation (10). Frame width of 2 mm. (b) Aberrated focal spot due to different phases: vertical discontinuity, boat phase and tilt plus astigmatism $(\phi(\rho) = \text{mod}(4\pi Z_1^1(\rho) + \pi Z_2^2(\rho), 2\pi))$. Frame width is 1 mm. (c) Aberrated focal spot due to tilting of the focusing lens. Frame width of 1 mm.

denotes the basis element and coordinates (X, Y) are changed to indices n, m. Also in the case of not integrating over the whole spectrum, equation (4) has to be discretized, which can be found in the supplementary document. The code for the simulation is provided in [22].

7. Results

Figure 3(a) shows the effect of the detector size for amplitude reconstruction in simulations for an amplitude with an encoded car image and different phase distributions in each row: Constant phase, π vertical discontinuity, boat image encoded in the basis and an encoded aberration of tilt and astigmatism aberration like that of figure 2(b). Along each column the amount of the sampling of the Fourier space increases. In the case of a constant phase (first row), no difference in the detector size is noticeable. However, already the split phase case (second row) introduces a vertical line in the DC term that is also present in when sampling 25% of the spectrum. The boat phase (third row) disappears at 50% coverage. Finally (fourth row), the Zernike aberration is persistent even at 75% and only disappears completely when the detector covers the full Fourier spectrum.

Figure 4(a) presents the results of the reconstructed amplitude for the experiment using the same car amplitude with the

same phase profiles encoded by the SLM. The columns feature different detector sizes that correspond to a certain amount of the Fourier spectrum. In all cases the results are similar to the simulation but there is more noise. For example, the most extreme case of the tilt and astigmatism aberration (fourth row) the phase has more contrast than in the simulation and it is still noticeable at 75% of the integrated Fourier spectrum. In order to quantify the similarity of the reconstructed amplitude images, we use 1- the root means square error (RMSE), where the reference image is the one that is reconstructed with a detector that spans over $2r_k$. The RMSE ranges between [0,1], where 0 is a small error. Since the values approach zero very fast, we chose 1 - RMSE to achieve a better visualization for concordance of images. Figures 3(b) and 4(b) plot the similarity against the relative detector size for the simulations and experiments, respectively. In general, the graphs follow a very similar course for the used phase distributions, where more complex phase distributions require a larger percentage of the Fourier space sampling in order to reach higher similarities. Interestingly, the simulations (figure 3(c)) reach a similarity of 99% at a detector size of r_k , i.e. the detector spans over 50% of the Fourier spectrum. In contrast, the similarity index for the experimental data is generally lower, due to noise in the measurements, but values are in the same range and follow the same course. Here, a similarity index >95\% is reached for detector sizes that cover over 50%–75% of the Fourier spectrum.

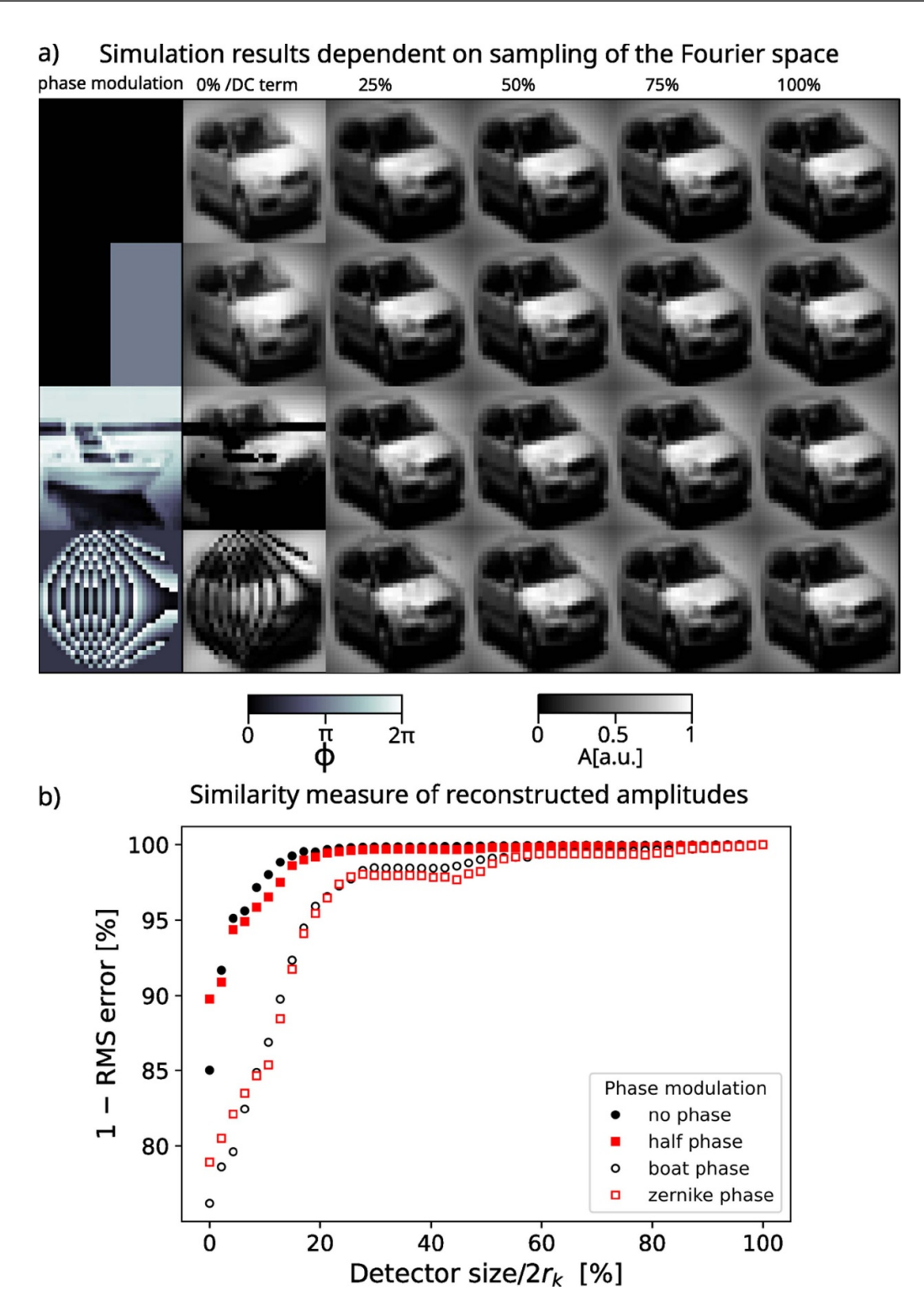


Figure 3. Reconstructed amplitude dependent on the sampling size of the Fourier spectrum with single pixel imaging. (a) Simulation results and (b) similarity (1- RMS error) of the reconstructed amplitudes dependent on the sampling size of the Fourier spectrum. Major effects of aberrations disappear when sampling over 50% of the Fourier spectrum and completely disappear when the full spectrum is sampled.

In order to demonstrate an applied case of aberrations that can occur in typical experimental setups, like misalignment of optical elements, we apply a tilt to the focusing lens. This tilt in the experiment can be modeled by a composition of Zernike polynomials $\phi(\rho) = \text{mod}(5\pi Z_1^1(\rho) + n\pi Z_2^2(\rho), 2\pi)$,

where n defines the degree of the tilt. We simulate the experimental tilt by choosing n=5 and n=30 for the 5° and 10° tilt, respectively. The effective aperture of the beam emerging from the SLM is much smaller than the aperture of the optical elements. In the simulations the field is defined

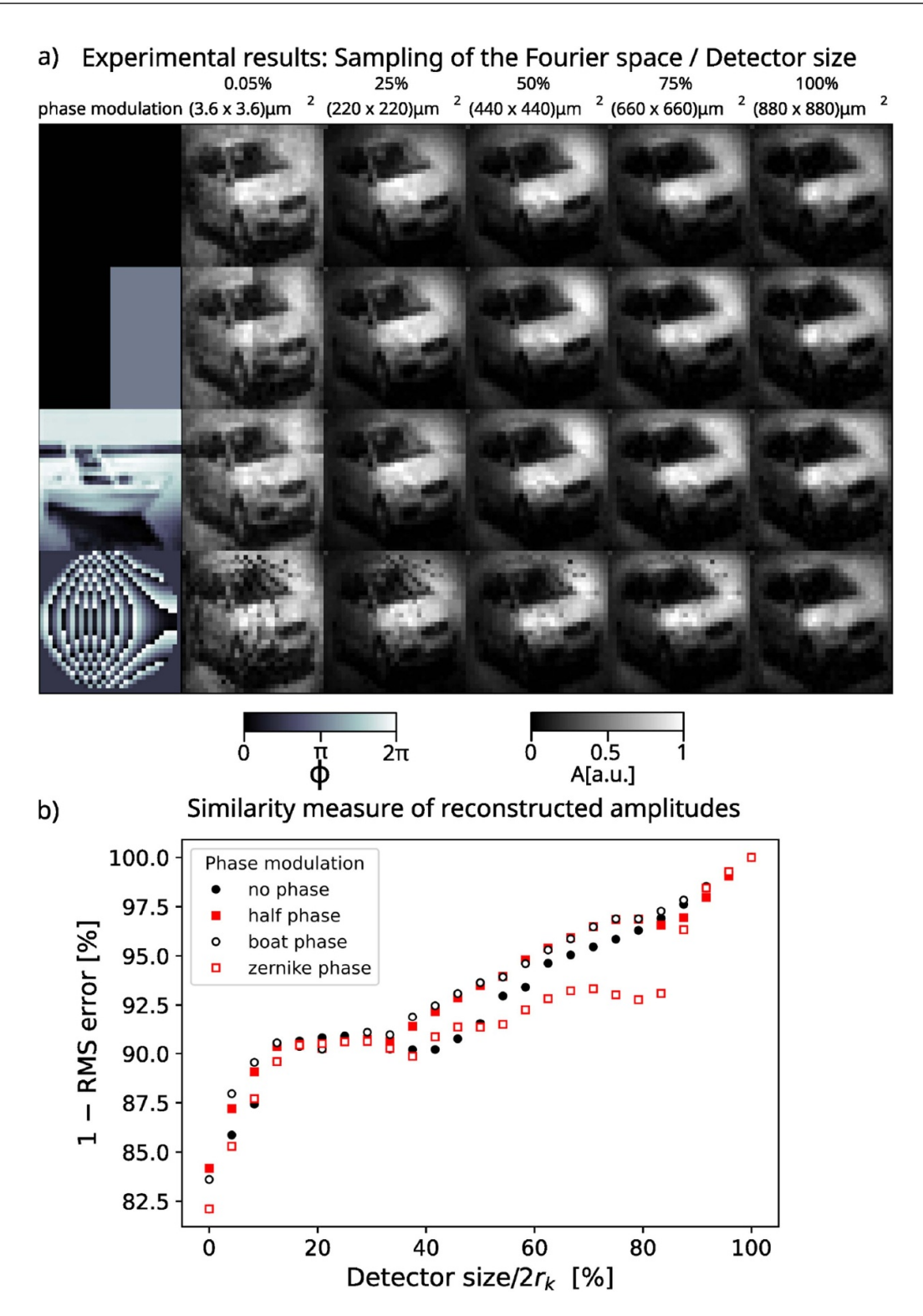


Figure 4. Reconstructed amplitude dependent on the sampling size of the Fourier spectrum with single pixel imaging. (a) Experimental results and (b) similarity (1- RMS error) of the reconstructed amplitudes dependent on the sampling size of the Fourier spectrum. Major effects of aberrations disappear when sampling over 50% of the Fourier spectrum and completely disappear when the full spectrum is sampled.

in the same spatial grid where the field is encoded at the SLM.

Figures 5(a) and 6(a) show simulated and experimental single pixel amplitude images of the Gaussian laser beam (no amplitude or phase encoding at the SLM). The case with a

car image encoded in the amplitude is shown in figures 5(b) and 6(b) for simulations and experiments, respectively. In all (figures 5 and 6) the rows represent different degrees of tilt of the collecting lens: 0° , 5° and 10° (cmp. to figure 2(c)), while the detector size increases along the columns. For all cases,

Simulation of twisted lens

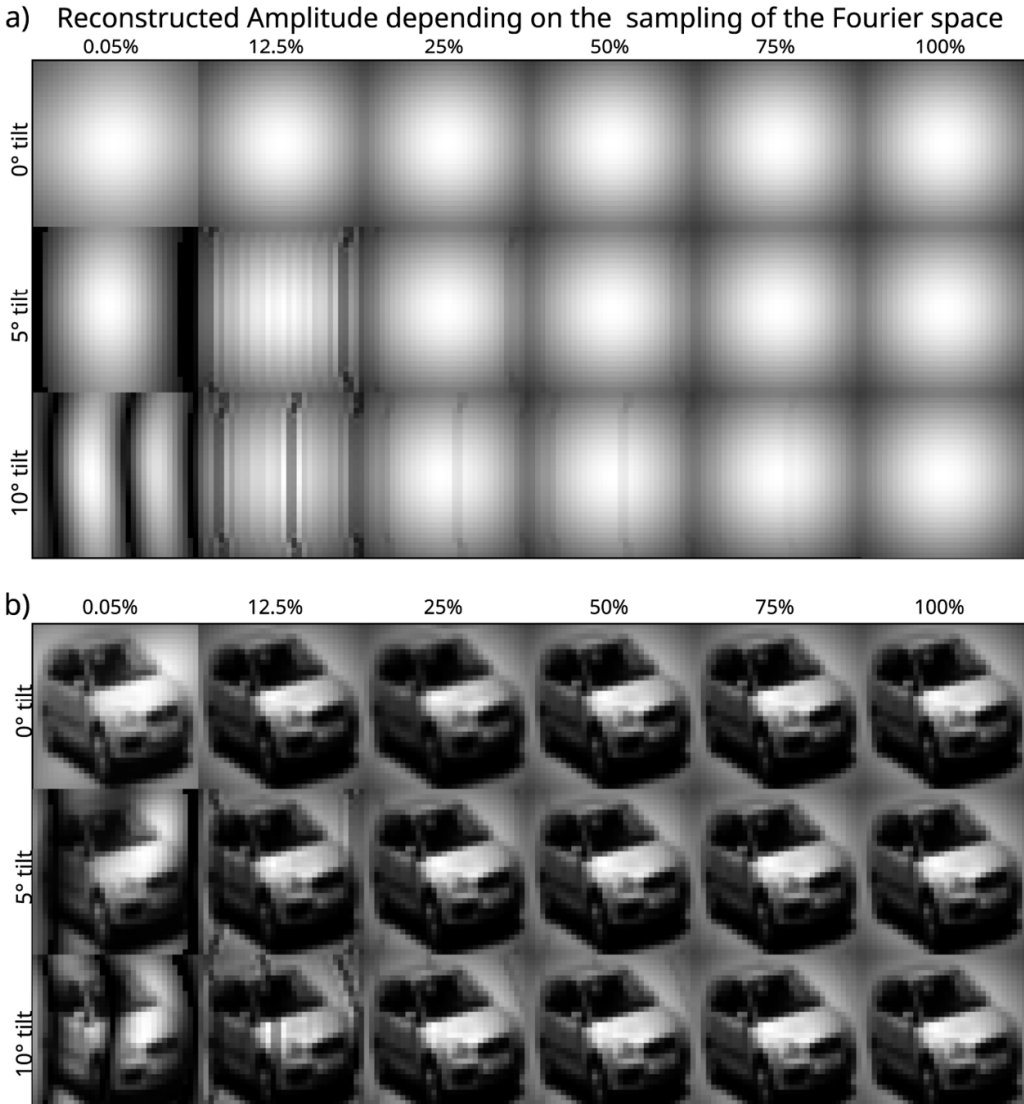


Figure 5. Simulation: reconstructed amplitude using single pixel imaging with a titled lens dependent on the detector size. (a) No amplitude modulation Gaussian beam, (b) amplitude modulated with a 'car' image. Data for 0° tilt is the same as for the first row of figure 3(b).

no change in the acquired image is apparent when the lens is perpendicular towards the optical axis—that is, no aberrations are introduced into the field. However, already a slight tilt of 5° is noticeable for small detector sizes 3.6 μ m (0%–0.5% $2r_k$) and 110 μ m (12.5% $2r_k$) as dark vertical lines appear close to the border. Note, that the observed vertical lines are of very close resemblance in both the simulations and the experiment, implying that they are caused by the Zernike phase aberration of the tilt. Increasing the tilt to 10° introduces two slightly bent vertical lines on the right border for detector sizes that sample up to 25% of the Fourier spectrum. At 50% the recovered amplitude still features a shadow on the right side and is indistinguishable after sampling 75% of the Fourier spectrum. Notice, that these vertical lines are mainly an effect of the tilting of the lens, as the beam has a square size of ≈ 2.3 mm, while the circular aperture of the lens has a diameter of 2.56 cm. The beam is centered in the lens, so that spherical aberrations and effects of the aperture are minimal and only the tilt and astigmatism remain as sources of aberration, which is similar to the Zernike Polynomial presented in figures 2–4.

8. Conclusion

We have shown the importance of the bucket detector size in SPI with a coherent light source as a function of the light projection system. In order to cover the full Fourier spectrum it is important that the detector has an effective diameter of $2r_k = \lambda f/a$, determined by the focal length f and superpixel size of the measurement basis a. For a detector that has a size of less than between 50% and 75% of $2r_k$, the phase distribution is visible in the reconstructed image.

Conventional photodiodes can have large sizes on the order of 10 mm, while fast photodiodes have smaller dimensions in

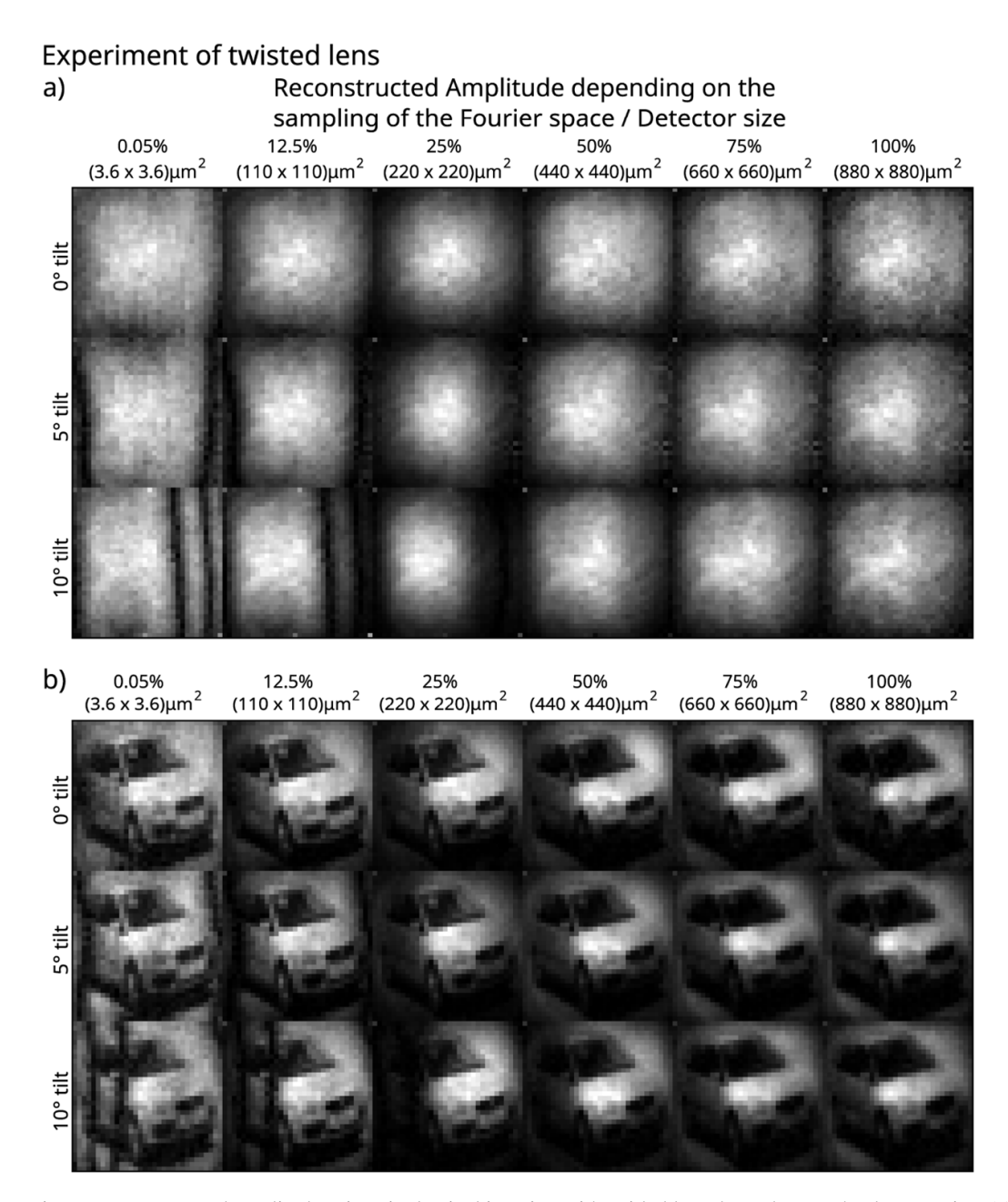


Figure 6. Experiment: Reconstructed amplitude using single pixel imaging with a titled lens dependent on the detector size. (a) No amplitude modulation, (b) amplitude modulated with a 'car' image. Data for 0° tilt is the same as for the first row of figure 3(b).

the range of a few tens to few hundreds of micrometers. An extreme case would be that of coupling the light to a single mode optical fiber that is very sensitive to the input mode and hence will have large losses when coupling most of the projected Hadamard basis elements that do not focus at a single spot. For such cases, the effect of crosstalk with the phase could be very important in applications where the phase varies rapidly, such as image transmission through biological or random media [23] where light interacts with microstructures, so that a randomized phase distribution can appear in the transmitted image. Note, that the described effects only occur for a coherent light source. Using an incoherent light source (i.e. thermal or broad-band) bypasses this effect. To summarize the results: We have shown that for coherent light

in SPI there can be phase cross talk with the amplitude that emerges only from the bucket detector measurement without interferometry. This has been observed in complex encoding (amplitude and phase) of laser fields with SLMs or DMDs [20, 24] and now has been observed in the context of SPI and CGI.

Data availability statement

The data that support the findings of this study are openly available at the following URL/DOI: https://github.com/Denbo313/Errors-in-single-pixel-photography-emerging-from-light-collection-limits-by-the-bucket-detector.

Acknowledgments

We acknowledge support from the UNAM-PAPIIT Grants IN107222; CTIC-LANMAC; CONAHCYT LN-299057 and CF-2023-I-657.

ORCID iDs

Dennis Scheidt https://orcid.org/0009-0008-1035-9574 Pedro A Quinto-Su https://orcid.org/0000-0002-8363-3932

References

- [1] Duarte M F, Davenport M A, Takhar D, Laska J N, Sun T, Kelly K F and Baraniuk R G 2008 Single-pixel imaging via compressive sampling *IEEE Signal Process. Mag.* 25 83–91
- [2] Candes E, Romberg J and Tao T 2006 Robust uncertainty principles: exact signal reconstruction from highly incomplete frequency information *IEEE Trans. Inf. Theory* 52 489–509
- [3] Sun M-J and Zhang J-M 2019 Single-pixel imaging and its application in three-dimensional reconstruction: a brief review Sensors 19 732
- [4] Strekalov D V, Sergienko A V, Klyshko D N and Shih Y H 1995 Observation of two-photon 'ghost' interference and diffraction *Phys. Rev. Lett.* 74 3600–3
- [5] Pittman T B, Shih Y H, Strekalov D V and Sergienko A V 1995 Optical imaging by means of two-photon quantum entanglement *Phys. Rev.* A 52 R3429–32
- [6] Clemente P, Durán V, Tajahuerce E, Torres-Company V and Lancis J 2012 Single-pixel digital ghost holography *Phys. Rev.* A 86 041803
- [7] Padgett M and Boyd R 2017 An introduction to ghost imaging: quantum and classical *Phil. Trans. R. Soc.* A **375** 20160233
- [8] Gong W 2022 Performance comparison of computational ghost imaging versus single-pixel camera in light disturbance environment *Opt. Laser Technol*. 152 108140
- [9] Liu R, Zhao S, Zhang P, Gao H and Li F 2019 Complex wavefront reconstruction with single-pixel detector *Appl. Phys. Lett.* 114 161901
- [10] Ota K and Hayasaki Y 2018 Complex-amplitude single-pixel imaging Opt. Lett. 43 3682–5
- [11] Zupancic P, Preiss P M, Ma R, Lukin A, Tai M E, Rispoli M, Islam R and Greiner M 2016 Ultra-precise holographic

- beam shaping for microscopic quantum control *Opt. Express* **24** 13881–93
- [12] Sephton B, Nape I, Moodley C, Francis J and Forbes A 2023 Revealing the embedded phase in single-pixel quantum ghost imaging *Optica* 10 286–91
- [13] Scheidt D and Quinto-Su P A 2024 Spatial resolution limit of single pixel imaging of complex light fields *Opt. Lett.* 49 2381–4
- [14] Jauregui-Sánchez Y, Clemente P, Carmona P, Tajahuerce E and Lancis J 2018 Signal-to-noise ratio of singlepixel cameras based on photodiodes *Appl. Opt.* 57 B67–B73
- [15] Sun M-J, Xu Z-H and Wu L-A 2018 Collective noise model for focal plane modulated single-pixel imaging *Opt. Lasers Eng.* 100 18–22
- [16] Goodman J W 2017 Introduction to Fourier optics Introduction to Fourier optics ed J W Goodman vol 1 3rd edn (Roberts & Co. Publishers)
- [17] Scheidt D, Arzola A V and Quinto-Su P A 2023 Shaping the angular spectrum of a Bessel beam to enhance light transfer through dynamic strongly scattering media *Opt. Lett.* 48 6360-3
- [18] Krizhevsky A, Hinton G 2009 Learning multiple layers of features from tiny images *Technical Report* (University of Toronto)
- [19] Bolduc E, Bent N, Santamato E, Karimi E and Boyd R W 2013 Exact solution to simultaneous intensity and phase encryption with a single phase-only hologram *Opt. Lett.* 38 3546–9
- [20] Chen Q, Shen X, Cheng Y, Liu J, Cai J and Liu Y 2021 A crosstalk-reduced method of complex fields encoding using a single phase-only spatial light modulator *Optik* 228 166190
- [21] Scheidt D and Quinto-Su P A 2023 Comparison between Hadamard and canonical bases for *in situ* wavefront correction and the effect of ordering in compressive sensing *J. Opt. Soc. Am.* A 40 45–52
- [22] Scheidt D, Quinto-Su P 2024 Supplementary data and code for errors in single pixel photography emerging from light collection limits by the bucket detector (available at: https:// github.com/Denbo313/Errors-in-single-pixel-photographyemerging-from-light-collection-limits-by-the-bucketdetector)
- [23] Tajahuerce E, Durán V, Clemente P, Irles E, Soldevila F, Andrés P and Lancis J 2014 Image transmission through dynamic scattering media by single-pixel photodetection Opt. Express 22 16945–55
- [24] Persson M, Engström D and Goksöor M 2012 Reducing the effect of pixel crosstalk in phase only spatial light modulators Opt. Express 20 22334–43